Stem Cell Reports
Article

ISSCR

OPEN ACCESS

Deep neural net tracking of human pluripotent stem cells reveals intrinsic behaviors directing morphogenesis

David A. Joy,[1,2] Ashley R.G. Libby,[2,3] and Todd C. McDevitt[2,4,*]
[1]UC Berkeley-UC San Francisco Graduate Program in Bioengineering, San Francisco, CA, USA
[2]Gladstone Institutes, San Francisco, CA, USA
[3]Developmental and Stem Cell Biology PhD Program, University of California, San Francisco, San Francisco, CA, USA
[4]Department of Bioengineering and Therapeutic Sciences, University of California, San Francisco, San Francisco, CA, USA
*Correspondence: todd.mcdevitt@gladstone.ucsf.edu
https://doi.org/10.1016/j.stemcr.2021.04.008

SUMMARY

Lineage tracing is a powerful tool in developmental biology to interrogate the evolution of tissue formation, but the dense, three-dimensional nature of tissue limits the assembly of individual cell trajectories into complete reconstructions of development. Human induced pluripotent stem cells (hiPSCs) can recapitulate aspects of developmental processes, providing an *in vitro* platform to assess the dynamic collective behaviors directing tissue morphogenesis. Here, we trained an ensemble of neural networks to track individual hiPSCs in time-lapse microscopy, generating longitudinal measures of cell and cellular neighborhood properties on timescales from minutes to days. Our analysis reveals that, while individual cell parameters are not strongly affected by pluripotency maintenance conditions or morphogenic cues, regional changes in cell behavior predict cell fate and colony organization. By generating complete multicellular reconstructions of hiPSC behavior, our tracking pipeline enables fine-grained understanding of morphogenesis by elucidating the role of regional behavior in early tissue formation.

INTRODUCTION

In the developing embryo, individual cells undergo a sequence of cell fate transitions and migration events to cooperatively form the tissues and structures of the organism. Cell-tracking techniques based upon high-resolution imaging have been used to trace cell lineage and describe the emergent patterns of embryogenesis across multiple model organisms (Chhetri et al., 2015; Peng et al., 2016; Sulston et al., 1983), including the early human pre-implantation embryo (Deglincerti et al., 2016; Shahbazi et al., 2016). However, automated tracking of cell migration within whole embryos *in vivo* has been limited both in size to small organisms such as *C. elegans* (Bao et al., 2006), due to the difficulty of identifying and tracking cells in a crowded multicellular environment, and in scale, due to the low throughput of 3D imaging and reconstruction techniques (Stegmaier et al., 2016). Researchers frequently address the problem of density by employing sparse labeling of cells, either by tracing only cells of a single lineage (Cai et al., 2013; Henner et al., 2013) or by detecting transcriptional (Lou et al., 2014) or morphologic distinctions between cells (Stegmaier et al., 2016). Similarly, in the analysis of cell behavior *in vitro*, experimental limitations such as mechanical confinement to 1D tracks (Maiuri et al., 2012) or sparse labeling (Libby et al., 2018) have been required to accurately track individual cells, limiting the ability of these systems to monitor multicellular tissue behaviors with comprehensive single-cell resolution.

Self-organizing developmental processes are often initiated by small founder populations within a larger population of physically interconnected cells, as in the case of classic Turing patterns (Turing, 1952). Similar multicellular organizational events have been observed *in vitro* with human induced pluripotent stem cells (hiPSCs), revealing their heterogeneous differentiation potential due to global positional cues (Warmflash et al., 2014), cell population boundaries (Libby et al., 2018), or cell-cell interactions (Hookway et al., 2016). In particular, because cell fate and function are strongly influenced by local interactions within multicellular networks (Malmersjo et al., 2013; Novkovic et al., 2016; White et al., 2013), coordinated morphogenic processes exhibit scale-free connectivity (i.e., at multiple scales, cell behavior is coordinated through a central hub of influential cells) (Barabási et al., 1999), indicating that small populations of cells, by establishing highly connected organizing centers, can exert a large impact on the final composition of the developing tissue (Martinez Arias and Steventon, 2018; Shahbazi and Zernicka-Goetz, 2018). Sparse labeling approaches inherently undersample these rare populations, highlighting the need for dense cell-tracking algorithms to definitively identify the origins and quantify the behaviors of organizers.

Recent advances in machine learning, in particular in deep neural networks, have demonstrated superhuman performance at image segmentation, revolutionizing the field of computer vision (LeCun et al., 2015; Moen et al., 2019). Several classes of convolutional neural nets

(CNNs) have been developed specifically to perform dense cell segmentation (Xie et al., 2016), based upon different architectures such as autoencoders (Su et al., 2015), U-Nets (Falk et al., 2019; Ronneberger et al., 2015; Xie et al., 2018), or variants of the Inception architecture (Cohen et al., 2017; Szegedy et al., 2014). Recent approaches have further enhanced cell-tracking fidelity by combining deep cell bounding-box detection with ancillary tasks such as morphology classification (He et al., 2017) or mitosis detection (Wang et al., 2019), improving accuracy, although requiring additional annotation. Further, preprocessing and filtering steps to rapidly reject irrelevant images (Araújo et al., 2019) have enabled highly scalable deep cell segmentation pipelines. Applying adaptive tracking algorithms such as particle filters (He et al., 2017; Wang et al., 2019) has enabled cell tracking under conditions of high morphological diversity and low image resolution, although the impact of cell density on tracking fidelity was not examined. In contrast, Hiramatsu et al. (2018) developed a novel pipeline where individual U-Net CNNs, each trained independently, were combined using a gating network to produce a high-quality, dense cell segmentation, although the impact of neural net architecture on the final result was not explored. Each pipeline offers distinct trade-offs between cell segmentation accuracy, training efficiency, noise robustness, and computational complexity, with sub-optimal network choice leading to reduced tracking quality and poor capture of cell behavior. While cell-tracking algorithms have historically been assessed through head-to-head competitions (Caicedo et al., 2019; Ulman et al., 2017), the potential advantage of combining complementary neural net architectures for cell localization and tracking has yet to be rigorously examined.

In this study, we overcame the challenge of dense cell tracking by developing an ensemble of three neural networks (FCRN-B, Xie et al., 2016; Count-ception, Cohen et al., 2017; and a Residual U-Net, Xie et al., 2018) to localize each individual cell nucleus in an hiPSC colony. Nuclei displacements were then connected between sequential frames of a time series, enabling high spatiotemporal resolution of hiPSC behaviors over relevant developmental timescales of hours to days. This dense cell-tracking pipeline revealed distinctive cell behaviors based on location within the colony, cell heterogeneity, and response to extracellular signaling molecules. Long-term cell tracking in combination with immunostaining for lineage markers enabled tracking of the differentiation history of colonies with single-cell resolution. The whole-colony tracking and analysis pipeline revealed radially stratified shifts in cell migration speed and cell packing density in hiPSC colonies in reaction to changes in culture conditions. Changes in cellular behavior were detected at the local cell neighborhood level in response to differentiation induced by externally applied morphogens, enabling real-time identification of local organizing centers (~10–20 cells) that precede tissue-scale morphogenic events. By detecting rare organizational events, our computational cell-tracking pipeline allows for a more comprehensive dynamic understanding of the multicellular principles of morphogenesis, which can empower more refined control of organoid and engineered tissue development.

RESULTS

Manual annotation of cell migration in hiPSC colonies

Human iPSCs form dense, multilayered colonies *in vitro* with indistinct boundaries between cells when using common phase imaging, pan-cytoplasmic, or pan-nuclear staining techniques. To establish a baseline for cell localization quality, a series of heterogeneously labeled colonies was generated by mixing wild-type hiPSCs with an hiPSC-derived cell line expressing a nuclear GFP fluorescent label (Lamin-B:GFP) at ratios of 9:1 (10% labeled), 7:3 (30% labeled), or 0:10 (100% labeled). While the cells were maintained in pluripotency media, mixtures were force aggregated in microwells (Hookway et al., 2016), allowed to reattach to tissue-culture plates, and then imaged every 5 min for 6 h to generate a set of frames for annotation (Figures 1A and 1B). Seven individual human annotators selected the center of every GFP-positive cell nucleus in 12 sequential pairs of 500-cell colonies containing 10%, 30%, or 100% Lamin-B:GFP hiPSCs presented in randomized order. A spatial average of all seven annotation sets was calculated using k-means clustering to generate a ground truth human consensus segmentation for each frame (Figure 1C).

Human annotators were scored using a ratio of selected nuclei within a 5-μm radius from the consensus cell, divided by the total number of expected cells, missing cells, and incorrectly selected cells (true positives divided by all positives plus any false positives). The average individual rater reliability (IRR) was 88.5% (±7.9%), with a minimum of 83% and a maximum of 93% (Figure 1C). As a second comparison, the individuals and human consensus were rated on their ability to select the same cell twice in pairs of sequential frames. Average interframe reliability (IFR) was 85.8% (±7.7%), with a minimum of 75% and a maximum of 92% (consensus 90.2% ± 4.8%) (Figure 1D). To assess how increasing label density affected cell detection, performance metrics were stratified according to colony labeling density (Figure 1E). As expected, human annotators exhibited maximal IRR and IFR when evaluating colonies with the lowest percentage of GFP^+ cells (i.e., 10%), with performance significantly declining for

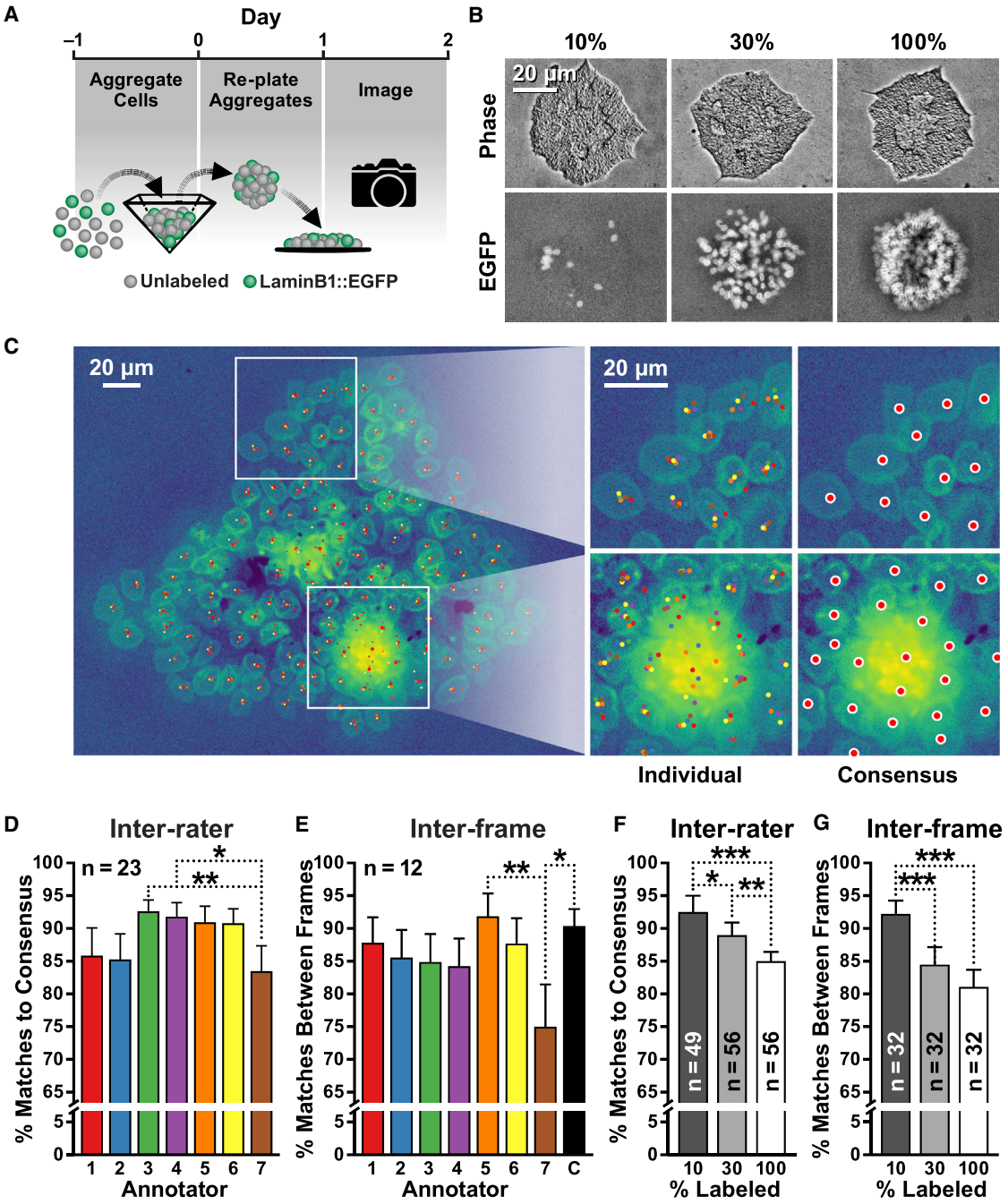

Figure 1. Quality of manual tracking plateaus with increasing density of labeled cells

(A) Schematic of imaging protocol where WTC11 and LaminB1:GFP cells were seeded into microwells at defined ratios of each population and then replated to form colonies.

(B) Colonies formed with 10%, 30%, and 100% LaminB1:GFP labeled cells.

(C) Individual annotator and consensus segmentations in sparser (top) and more dense (bottom) regions of the colony.

(D) Individual annotator accuracy compared with consensus for each image (n = 23 independent colonies) (*$p < 0.05$, **$p < 0.01$).

(E) Accuracy segmenting the same cell across sequential frames for all image pairs (n = 12 colony pairs) (*$p < 0.05$, **$p < 0.01$).

(F) Annotators accuracy compared with consensus on 10%, 30%, and 100% labeled colonies (n's are independent colonies per rater) (*$p < 0.05$, **$p < 0.01$, ***$p < 0.001$).

(G) Accuracy segmenting the same cell across sequential frames on 10%, 30%, and 100% labeled colonies (n's are colony pairs per rater) (***$p < 0.001$).

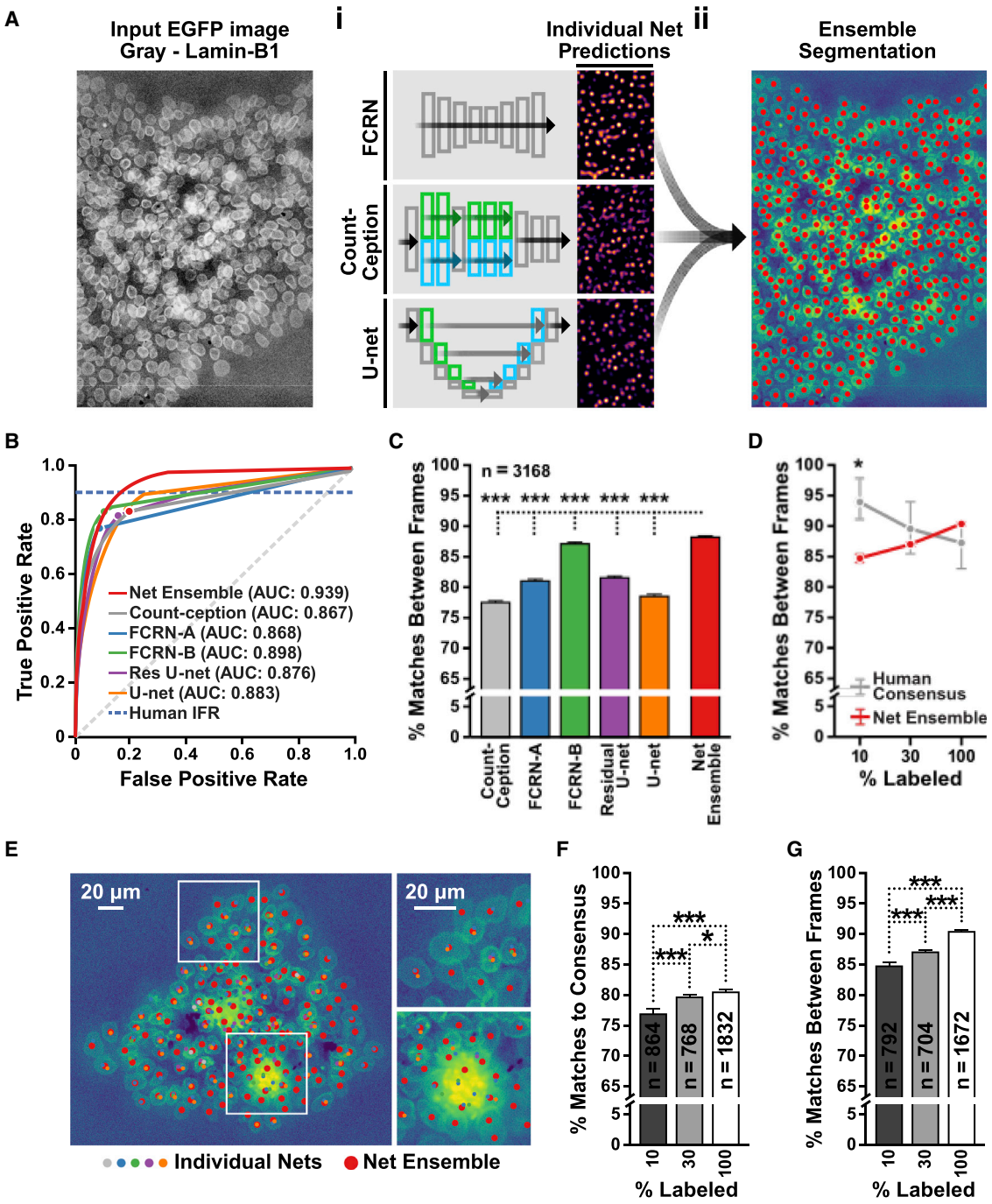

Figure 2. Heterotypic neural net ensembles generate human-quality segmentations

(A) (i) Input LaminB1:GFP images are segmented by multiple neural networks (FCRN-B, Residual U-Net, Count-ception), producing probability maps localizing the center of each LaminB1:GFP labeled nucleus. (ii) Consensus segmentation generated by a weighted average of these maps.

(B) The true-positive and false-positive rate for each segmentation and the area under the curve (AUC) for each architecture.

(C) Repeatability of cell detections between frames for the entire training set (n = 3,168 total frames, n = 37 independent colonies, ***$p < 0.001$ versus all single neural nets).

(D) Repeatability of cell detections, stratified by percentage labeling, compared with the human annotator consensus (n = 37 independent colonies) (*$p < 0.05$, 30% and 100% not significant).

(legend continued on next page)

colonies containing higher proportions of GFP$^+$ cells (30% and 100%).

To expand the dataset for neural network training, one annotator segmented 12 sequential frames of 24 colonies imaged on an inverted microscope at 20× magnification and 2 sequential frames of 32 colonies imaged on a confocal microscope at 10× magnification. Although this process generated ~500 MB of annotated data, it represented less than 2 h total of microscopy time, and approximately 2 workdays (14.8 h) of human annotation time, indicating that this annotation pipeline can be readily generalized to other cell types and live imaging modalities with relative ease.

Ensemble deep neural network segmentation of dense hiPSC colonies

To determine how deep neural networks compare with human segmentation performance, a diverse array of independent cell segmentation network architectures was selected from recent literature (Cohen et al., 2017; Ronneberger et al., 2015; Xie et al., 2016, 2018) (Figure 2A, i) and compared with the human annotator baseline as well as to the prediction of an ensemble of the selected architectures (Figure 2A, ii). Five different neural net architectures were compared, including two networks with VGG-like architecture (FCRN-A and FCRN-B, Xie et al., 2016), two U-Net architectures (U-Net, Ronneberger et al., 2015, and Residual U-Net, Xie et al., 2018), and an Inception-inspired network (Count-ception, Cohen et al., 2017). Each neural network was trained to segment the GFP images of 10%, 30%, and 100% labeled colonies by predicting a cone-shaped probability around the human annotated center of each nucleus. Despite architectural differences, all neural networks exhibited comparable average performance, segmenting the data with a receiver operating characteristic (ROC) area under the curve (AUC) of 0.86 or better (Figure 2B). Although no individual neural network was able to equal human segmentation of 100% GFP-labeled colonies, an ensemble of the three highest-performing networks surpassed human cell localization of fully labeled colonies (Figures 2A, ii, and 2B–2D). The primary variation between neural networks was due to spatial performance differences at the center or edge of individual colonies, with higher-quality segmentation in the denser, central regions of the colony and lower-quality segmentation at the edge (Figures 2E, S1C, and S1D).

Compared with the human annotator baseline, cell segmentation performance varied greatly between networks, with the two U-Net architectures agreeing least with human annotators, whereas FCRN-B and the ensemble agreed most often (Figure S1A). However, ROC AUC (Figure 2B) and effect size were often indistinguishable between similar architectures such as FCRN-A and FCRN-B (Cohen's $d = 0.11$) or U-Net and Residual U-Net ($d = 0.02$). Segmentation speed varied widely between architectures (from 23 to 288 ms per frame), but because the ensemble network was composed of several of the faster architectures, generating the composite segmentation was only 16.0% slower than using U-Net only (±2.5% slowdown; Figure S1B). In contrast to human annotators, neural net IRR and IFR segmentation accuracy improved with increasing label density (3.6% ± 0.4% and 5.7% ± 0.4%, Figures 2F and 2G, respectively). This increase in accuracy with increasing labeling density may reflect a bias in these neural networks toward more accurately segmenting regions of the colony with more labeled cells per field of view and hence more training signal, at the expense of sparser regions with fewer annotations.

Individual cell tracking of pluripotent stem cell behavior

Individual frame segmentations were initially combined using a nearest-neighbor linkage between frames to create cell tracks covering the center, middle, and edge regions of each colony (Figure 3A, blue, gold, and red regions, respectively), enabling construction of whole-colony traces for all cells in 100% GFP$^+$ colonies over the entire time series (Figure 3B). However, segmentation uncertainty at the individual cell level (e.g., a 95% accurate classifier will fail to detect a cell approximately once every 20th frame) led to fragmented cell tracks, which, upon manual inspection, were the result of loss of tracking of one to five frames for short periods, but which could be easily assigned to the same cell using neighborhood topology. To reduce random breakages, a second linking step was added to combine tails of track fragments across gaps of up to five frames, using the motion of the local cellular neighborhood to interpolate any missing cell positions. Neighborhood interpolation significantly increased track fragment lengths (from average coverage of 21.5% of the time series length to 33.5%, Figure S2A), bringing track fragment counts closer

(E) Representative image of individual and net ensemble detections, where each dot indicates the peak probability of a cell predicted by each neural net architecture.

(F) Agreement between net ensemble predicted labels and the human annotated dataset on 10%, 30%, and 100% labeled colonies (n's are frames of n = 37 independent colonies) (*p < 0.05, ***p < 0.001).

(G) Repeatability of the net ensemble detections over time compared across label percentages (n's are paired frames of n = 37 independent colonies) (***p < 0.001).

See also Figure S1.

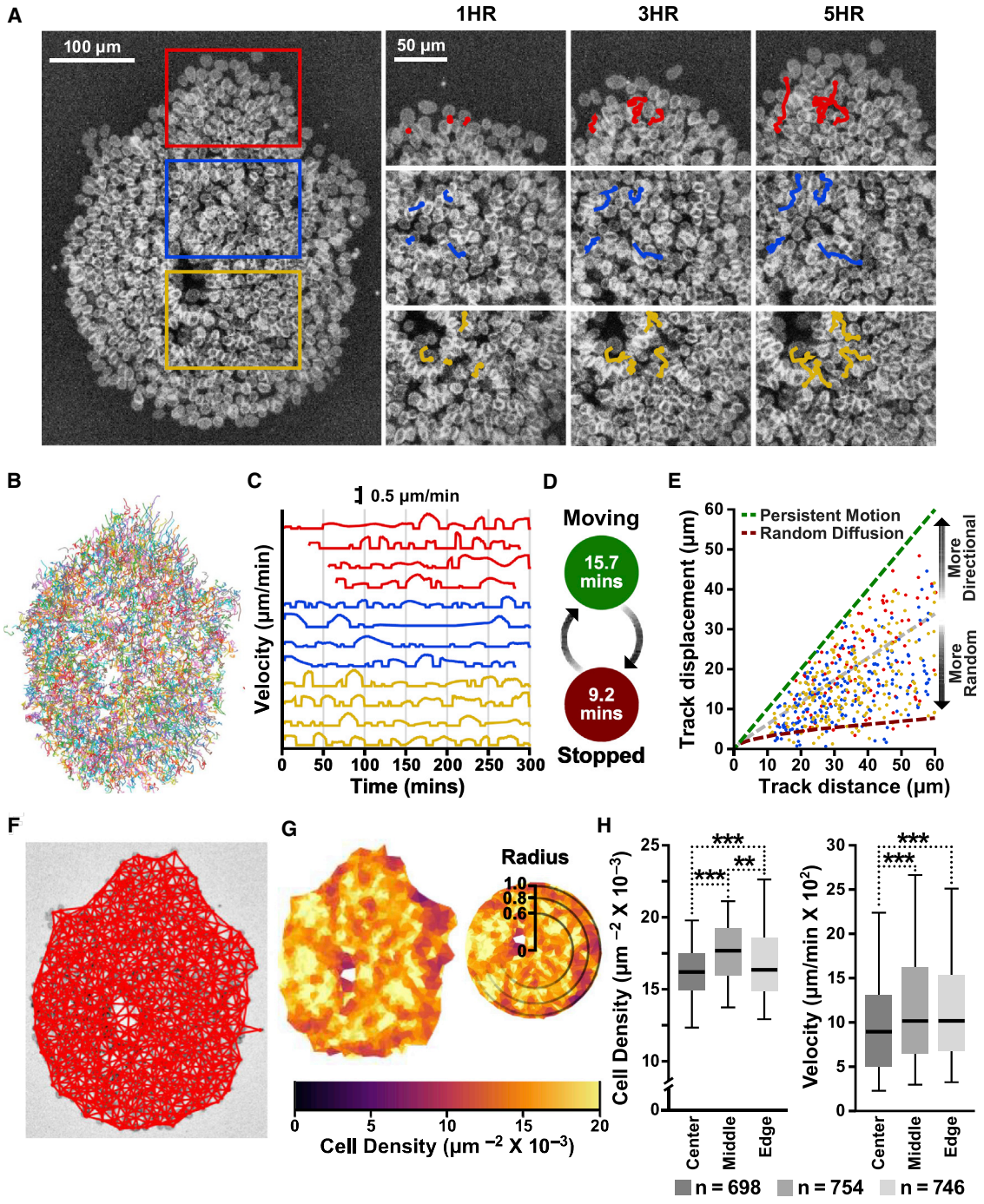

Figure 3. Spatiotemporal linkage of detections enables long-term single-cell tracking

(A) Depiction of example colony where regions were identified as center, middle, and edge (yellow, blue, and red, respectively).

(B) Dense track map created by linking detections covering the entire time series.

(C) Trace plot of example cell velocity tracks across colony locations (center, yellow; middle, blue; edge, red).

(D) Proposed two-state model of alternating active migration and quiescence fit from average active and stopped periods.

(E) Distribution of the ratio of total track displacement to total track distance, where colored dots represent individual tracks from the center, middle, and edge regions (yellow, blue, and red, respectively) and dotted lines show the theoretical curves for persistent migration (dark green) and random diffusion (dark red).

(F) Delaunay triangulation depicted across an example colony to calculate cell neighborhoods.

(legend continued on next page)

to the expected cell count based on cell seeding number and extrapolated growth rate: from 48.2% to 83.6% of individual cells fully tracked (n = 1,000 cells, Figure S2B).

To understand how individual cell behavior contributes to colony spreading and density, we calculated persistence of cell migration by locating regions of each track where the direction of cell motion changed by less than 5° per minute. Most cell tracks displayed clear binary switching between persistent migratory and stationary behavior (Figure 3C), with a mean active period of 15.7 min (± 12.7 min) followed by a quiescent period of 9.2 min (± 6.8 min), similar to the cyclic migration behavior observed in *E. coli* (Darnton et al., 2007) and eukaryotic cells (Devreotes and Janetopoulos, 2003) that can be attributed to the interaction between local polarizing cues and global inhibition of directional migration (Figure 3D). The active migration period was highest at the edge of colonies, and lowest at the center, while the quiescent period did not differ between colony regions (Figures S2C and S2D).

To measure the extent to which individual cells traveled directionally or diffused randomly, we calculated the ratio of track displacement to distance, where a value of 1.0 represents travel in a straight line, lower values represent an increasingly curved trajectory, and 0.0 represents a path that ultimately returns to its origin. Although cell tracks covered a broad range between purely directional and sub-diffusive (where directional cells approximated a linear relationship between displacement and diffusion, diffusive cells had a square-root relationship, and sub-diffusive cells had a lower than square-root relationship), there was no difference in directionality of motion between cells at the center, middle, or periphery of the colony (Figure 3E, blue, gold, and red points, respectively, Video S1). Finally, to identify coordinated movement between neighboring cells, we calculated the correlation between each cell's velocity vector profile and that of its immediate neighbors. In the center of colonies, nearest neighbors had uncorrelated velocity profiles (Pearson's R = 0.00298, SD 0.0757), whereas cells near the periphery demonstrated much higher correlation (R = 0.118, SD 0.383). This suggests that observed peripheral spreading results partially from multicellular collective migration, as has been shown previously in models of collective migration (Cui et al., 2005; Pegoraro et al., 2016), although the contribution of external forces (e.g., pressure from cell division in the colony interior) cannot be excluded. While the variability of cell behavior was high in all compartments, the large number of cell tracks enabled confident assessment of peripheral migratory bias, suggesting that dense cell tracking can elucidate otherwise subtle regional modulations to stochastic random walks.

To analyze the dynamic behavior of hiPSC colonies, a graph structure of each colony was created using Delaunay triangulation (Figure 3F). Based on the triangulation, individual cell area was estimated using the average of all triangles surrounding a cell within an empirically derived maximum link distance threshold of 50 μm (Figures 3G, S3E, and S3F), although this value is easily tuned for other epithelial cell types with different characteristic spacing. The local cell density was then approximated as the inverse of this triangulated cell area. The entire colony mesh and all cell measurements, such as density or velocity, were mapped onto the unit circle and then separated into three rings of equal area corresponding to the center, middle, and periphery of the colony (Figure 3G). In pluripotent colonies, cells in the peripheral region were packed less densely relative to the middle and central bins ($p < 0.001$, $d > 0.2$) (Figure 3H), suggesting that local crowding effects contribute to radial inhomogeneities in cell packing in hiPSC colonies. In contrast, cells in the middle and peripheral bins moved faster than cells in the center ($p < 0.001$, $d > 0.19$) (Figure 3H), demonstrating an edge-biased cell migratory behavior and suggesting that colony compaction may play a role in hiPSC colony spreading, as has been reported for migration of other epithelial cells (Cui et al., 2005; Pegoraro et al., 2016).

Packing and migratory behaviors of undifferentiated pluripotent stem cells

To interrogate the heterogeneous behavior of hiPSC colonies, we compared standard pluripotency maintenance conditions using the CNN tracking algorithm. First, we compared the effect of colony size on single-cell behavior by forming colonies of either 100 or 500 cells (Figure 4A, i). The average cell density and travel distance of 100-cell colonies were more similar to those of the edge of 500-cell colonies than to the center, suggesting that 100-cell colonies uniformly exhibit a similar organization and behavior compared with the edge of 500-cell colonies (Figure 4A, ii). At both colony sizes, cells at the edge displayed longer travel distances and higher migration speeds than those at the center (Figures 4A, iii and iv, and S3A). One hundred-cell colonies were more uniform in both density and distance traveled, with both measures closer to the

(G) Average inverse area of Delaunay triangles around each cell (cell density) depicted on the example colony and projected onto the unit circle.

(H) Quantification of cell density and velocity across the colony region identified by projecting triangulated cell positions onto rings of the unit circle (n's are cells from the representative colony shown) (**$p < 0.01$, ***$p < 0.001$).

See also Figure S2.

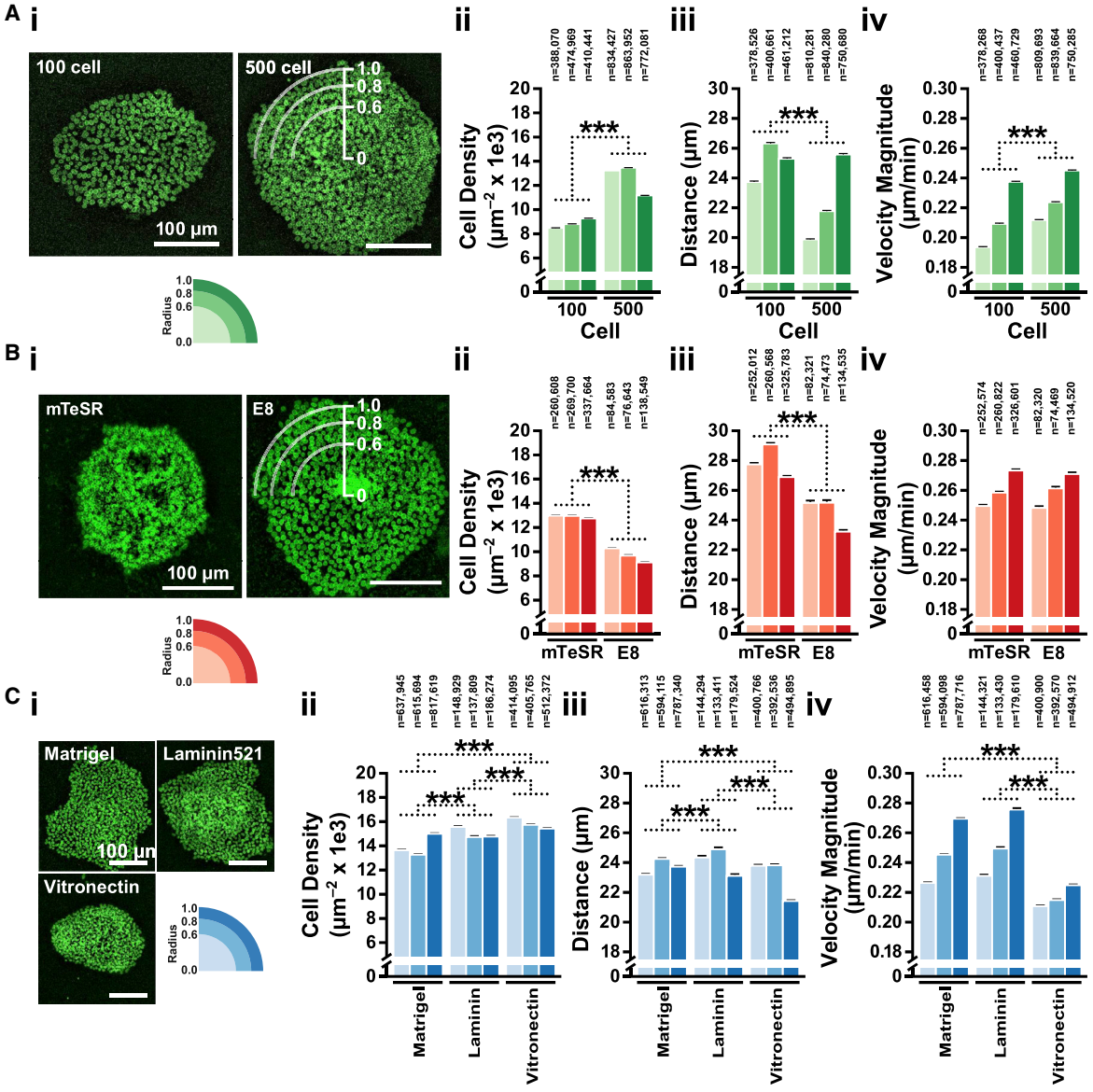

Figure 4. Basal culture conditions change cell packing density and migratory behavior

(A) (i) Example images of colonies with 100 or 500 starting cells. Comparison of 100-cell and 500-cell colonies stratified by colony region for: (ii) average cell density (***$p < 0.001$), (iii) average total cell distance traveled in 6 h (***$p < 0.001$), and (iv) average instantaneous cell velocity (***$p < 0.001$, n's refer to total cell counts of n = 20/20 100-cell/500-cell independent colonies, respectively, with cells stratified by normalized colony radius; colors from light to dark reflect center to edge).

(B) (i) Example images of colonies generated from cells cultured in mTeSR or E8. Comparison of mTeSR and E8 colonies stratified by colony region for: (ii) average cell density (***$p < 0.001$, n's refer to total cell counts of n = 16/16 mTeSR/E8 independent colonies, respectively), (iii) average total cell distance traveled in 6 h (***$p < 0.001$), and (iv) average instantaneous cell velocity (not significantly different).

(C) (i) Example images of colonies adhered to Matrigel-, vitronectin-, or rLaminin-521-coated plates. Comparison of Matrigel, vitronectin, and rLaminin-521 colonies stratified by colony region for: (ii) average cell density (***$p < 0.001$, n's refer to total cell counts of n = 33/35/17 Matrigel/vitronectin/rLaminin-521 independent colonies, respectively), (iii) average total cell distance traveled in 6 h (***$p < 0.001$), and (iv) average instantaneous cell velocity (***$p < 0.001$, Matrigel and rLaminin-521 not significantly different).

See also Figure S3.

cell density and travel values for the edge of 500-cell colonies. The transition in behavior from edge-like to center-like cells as confluency increases may account for the observed sensitivity of hiPSC pluripotency and differentiation to cell plating density (Lian et al., 2013) and colony size (Warmflash et al., 2014).

Next, we explored the effect of pluripotency maintenance media on colony behavior by comparing the effect of passaging hiPSCs in mTeSR or E8 medium (Figure 4B, i). Colonies cultured in mTeSR were more compact, with frequent formation of multilayered structures and low-density regions in the center of the colony, while colonies cultured in E8 were uniformly flat with lower cell packing density (Figure 4B, ii). Individual cells within colonies cultured in E8 traveled less overall (Figure 4B, iii). Despite structural differences, cell migration velocities between the two conditions differed only slightly ($p = 0.012$, $d = 9.44 \times 10^{-3}$), indicating that the density shift could not be attributed solely to differences in cell motility between the two conditions (Figure 4B, iv, and S3B).

Finally, we interrogated changes in colony structure due to commonly used adhesive extracellular matrices, which have been shown to have a cell-extracellular matrix strain-mediated effect on hiPSC morphology, behavior, and differentiation potential (Przybyla et al., 2016). hiPSC aggregates were allowed to adhere to Matrigel, vitronectin, or recombinant Laminin-521 (rLaminin, Figure 4C, i). Cell adhesion was much lower on rLaminin, with only 47.2% of aggregates adhered after 24 h versus 91.7% on Matrigel and 97.2% on vitronectin. Cells in adherent colonies on both rLaminin and vitronectin had higher cell density than on Matrigel (Figure 4C, ii), while cells on Matrigel and rLaminin traveled longer distances in 6 h than on vitronectin (Figure 4C, iii). Cells on vitronectin had lower migration velocities, and much lower difference between center and edge migration velocities, than either Matrigel or rLaminin (Figures 4C, iv, and S3C). hiPSC behaviors on Matrigel and rLaminin were very similar for both cell migration distance and migration velocity; however, stratifying the colonies by radius revealed that colonies plated on Matrigel were 11.1% less dense in the center. hiPSCs in vitronectin colonies uniformly moved more slowly than those on other matrices, leading to more compact colony morphology overall. These results suggest that changes to substrate can subtly alter local cell behavior, providing a tool to subtly modulate peripheral migration or cell packing within hiPSC colonies.

Through dynamic characterization of hiPSC behavior, our tracking pipeline revealed that hiPSCs display a wide variety of heterogeneous behaviors while maintaining pluripotency. In particular, cells at the periphery of colonies exhibit an organization distinct from those in the center. The medium environment and substrate can modulate both static and dynamic aspects of the edge and center colony structure. However, static snapshots of colony configuration, such as cell density, do not predict dynamic cell behaviors such as cell migration distance or velocity. Since both static and dynamic cell behaviors prime hiPSCs toward particular differentiation trajectories (Glen et al., 2018; Libby et al., 2019; Przybyla et al., 2016; Warmflash et al., 2014), dynamic assessment of whole-colony behavior is necessary to illuminate the scope of hiPSC heterogeneity in pluripotency and predict priming during differentiation.

Lineage tracing of cell fate decisions during early morphogenic induction

We next assessed changes in hiPSC behavior during early lineage specification by employing our tracking pipeline to analyze differentiation protocols used to induce combinations of all three germ layers. Previous work has shown that multicellular annular ring patterns form during trilineage differentiation (Warmflash et al., 2014), but the dynamic changes to cell migration behavior during ring formation have not been described. In addition, protocols to induce either mesendoderm (Lian et al., 2013) or neuroectoderm (Chambers et al., 2009) have been reported, but whether those direct differentiation protocols induce dynamic transformations similar to those that occur during trilineage differentiation is not known. To monitor the transition from pluripotent cells to differentiating germ layers, a critical 24-h morphogenic window was identified for each differentiation protocol for further exploration.

In the BMP4-induced trilineage protocol (Figure 5A, i, Video S2), colonies adopted a round morphology 24 h after BMP4 treatment with relatively uniform velocity and cell density, consistent with undifferentiated colonies (Figure S3D). At 30 h post-induction, a small central region of higher cell density was detected, corresponding to the appearance of $EOMES^+$ cells (Figures S4A and S4B). Approximately 32 h after induction, cells across the colony slowed in migration velocity, except for a ring of cells at ~50% of the colony radius, which maintained similar velocity compared with undifferentiated cells (Figures 5A, ii, and S3E). In the center of the colony, cell density was constant for the entire period of observation; however, the periphery of the colony also began to rapidly decrease in cell density about 32 h post-induction, with a dense plateau of cells forming at approximately 50% of colony radius, consistent with previous reports (Tewary et al., 2017; Warmflash et al., 2014) (Figures 5A, ii, and S5A). All three germ lineages formed by 48 h, with $POU5F1^+$ ($OCT4^+$) cells in the center ring ($SOX2^-$, $EOMES^-$, presumptive endoderm), $EOMES^+$ cells in the middle (presumptive mesoderm), $SOX2^+$ cells at the colony edge ($OCT4^-$, $EOMES^-$, presumptive ectoderm), and the periphery of the colony negative for all

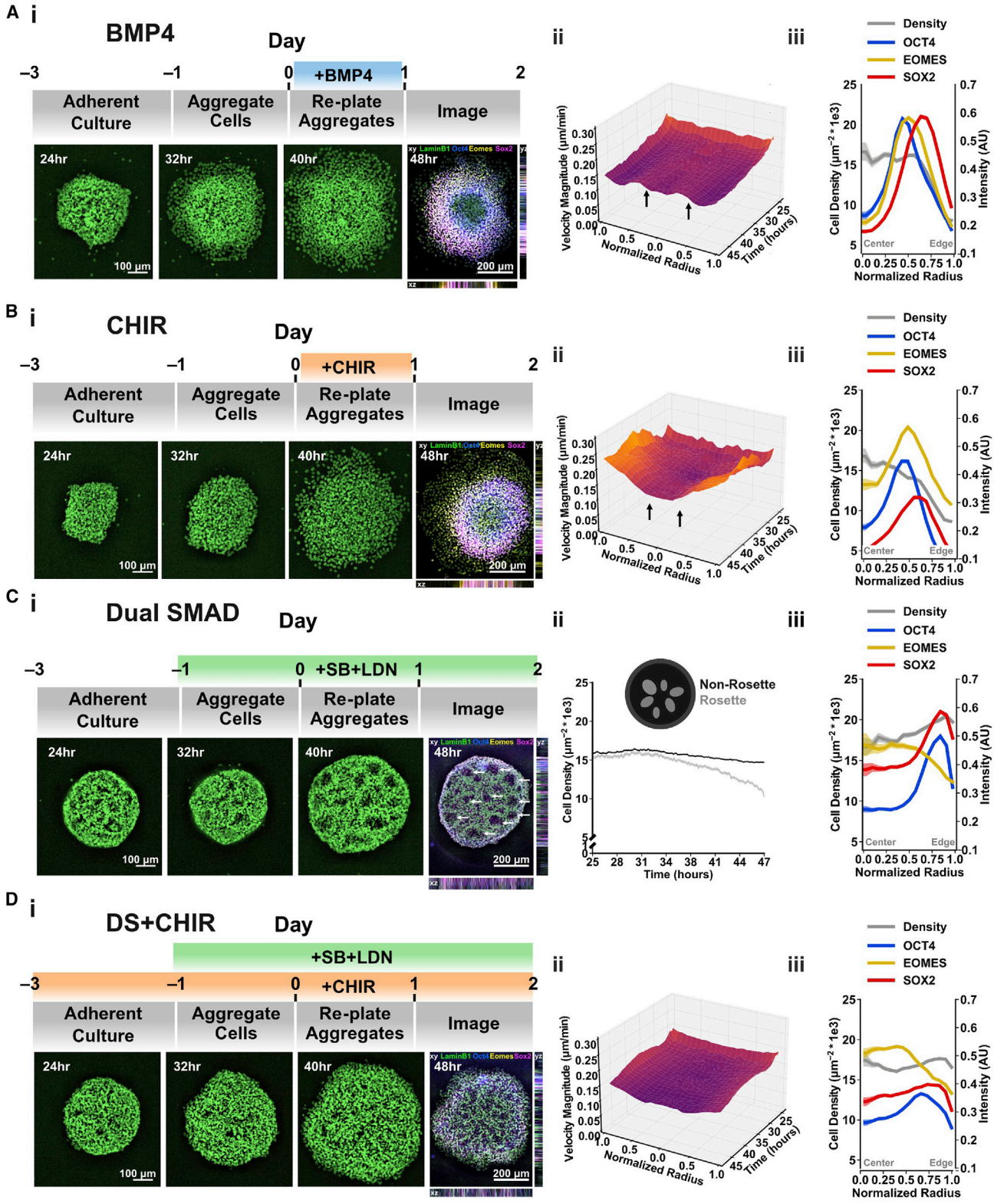

Figure 5. Whole-colony analysis reveals a density signature of multilineage differentiation

(A) (i) Treatment timeline and example time course of colony treated with BMP4 with example images at 24, 32, and 40 h post reseeding (HPR) and fixed and stained image of the same colony at 48 HPR. (ii) Surface plot of temporal evolution of average instantaneous cell

(legend continued on next page)

three markers (Figure 5A, iii). The transition between EOMES and SOX2 expression corresponded to both the maximum of cell migration velocity and the transition from high to low cell density, suggesting that the mesoderm ring acts as a migratory barrier between ectoderm and endoderm, enabling the physical phase separation of the colony into three distinct germ layers, analogous to gastrulation (Shahbazi and Zernicka-Goetz, 2018; Tewary et al., 2017; Warmflash et al., 2014).

Treatment with the WNT activator CHIR is commonly used to induce differentiation of mesoderm (Lian et al., 2013). Tall, multilayered colonies (average 61.4 ± 10.7 μm) formed after 24 h of 12 μM CHIR treatment and at 30 h stained uniformly for EOMES$^+$ cells (Figures S4C and S4D). By 48 h a secondary flat epithelial ring expanded radially out from the colonies, ultimately forming a stratified colony similar to that induced by BMP4 (Figure 5B, i, Video S3). Unlike BMP4-treated colonies, CHIR-treated cells at the colony periphery increased in migration speed by 50%, with individual cells at the periphery of the colony undergoing epithelial to mesenchymal transition and traveling beyond the field of view (Figure S5G). Similar to BMP4 treatment, the central region maintained cell density similar to that of untreated colonies, while the middle and outer compartments rapidly decreased in density (Figures 5B, iii, and S5B). OCT4, SOX2, and EOMES were detected in all colonies, but levels of OCT4 and especially SOX2 were lower with CHIR than in BMP4-treated colonies, consistent with early CHIR induction directing differentiation toward mesoderm and away from neuroectoderm (Figure 5B, iii). Again, the peak of EOMES expression occurred at ~50% of the colony radius and the transition between EOMES and SOX2 regions corresponded spatially to the transitions from low to high velocity and high to low density, respectively. The direct comparison of CHIR- and BMP4-induced differentiations demonstrates that limited numbers of similar static snapshots of colony structure can mask distinctive cell behaviors that can indicate divergent differentiation trajectories of pluripotent cells.

Neuroectoderm-directed colonies remained behaviorally indistinguishable from untreated colonies through the first 48 h of dual SMAD inhibition. However, starting at 60 h after treatment, small rosettes of approximately 20 cells began to form ring structures that expanded continuously for the remaining 12 h of imaging (Figure 5C, i, and Video S4). Between 6 and 18 rosettes formed per colony (mean 10.1 ± 2.3) with a mean rosette diameter of 64.2 ± 21.1 μm. Rings consisting of regions of lower cell density began to appear 36 h after plating, with ring diameters expanding at a rate of 2.58 ± 0.51 μm/h and a mean center-to-center spacing between rings of 124.0 ± 27.5 μm (Figure 5C, ii). Average cell density was slightly higher at the periphery of colonies, corresponding to higher expression of both OCT4 and SOX2 (EOMES$^-$, potentially undifferentiated cells), while the center of the colonies expressed high SOX2 and low OCT4 (presumptive neuroectoderm, Figure 5C, iii). EOMES expression was slightly elevated in the center of the colonies, but overall EOMES was rarely detected compared with BMP4 or CHIR differentiation. None of the three lineage markers appeared to be specifically localized to the ring structures. Addition of CHIR pre-treatment (Libby et al., 2020) to the dual SMAD neuroectoderm protocol completely abrogated the formation of rosettes (Figure 5D, i, and Video S5). CHIR-pre-treated neuroectoderm colonies were indistinguishable from untreated colonies in both their uniform velocities and the radial distribution of cell densities (Figures 5D, ii and iii, S5I, and S5D, respectively). CHIR treatment elevated expression of EOMES, and suppressed expression of both SOX2 and OCT4, likely delaying the commitment of cells to

velocity over BMP4-treated colonies projected onto the unit circle (n = 16 independent colonies, arrows indicate the normalized radius of velocity transition). (iii) OCT4, SOX2, and EOMES expression profiles and average cell density profile at 48 HPR projected onto the unit circle in BMP4-treated colonies (n = 16 independent colonies).

(B) (i) Treatment timeline and example time course of colony treated with CHIR with example images at 24, 32, and 40 HPR and fixed and stained image of the same colony at 48 HPR. (ii) Surface plot of temporal evolution of average instantaneous cell velocity over CHIR-treated colonies projected onto the unit circle (n = 16 independent colonies, arrows indicate the normalized radius of velocity transition). (iii) OCT4, SOX2, and EOMES expression profiles and average cell density profile at 48 HPR projected onto the unit circle in CHIR-treated colonies (n = 16 independent colonies).

(C) (i) Treatment timeline and example time course of colony treated with dual SMAD inhibition at 24, 32, and 40 HPR and fixed and stained image of the same colony at 48 HPR with rosettes highlighted (white arrows). (ii) Temporal evolution of average cell density inside and outside of rosettes (n = 16 independent colonies). (iii) OCT4, SOX2, and EOMES expression profiles and average cell density profile at 48 HPR projected onto the unit circle in dual SMAD inhibition-treated colonies (n = 16 independent colonies).

(D) (i) Treatment timeline and example time course of colonies treated with both dual SMAD inhibition and CHIR pre-treatment at 24, 32, and 40 HPR with fixed and stained image of the same colony at 48 HPR. (ii) Surface plot of temporal evolution of average instantaneous cell velocity over dual SMAD + CHIR-treated colonies projected onto the unit circle (n = 16 independent colonies). (iii) OCT4, SOX2, and EOMES expression profiles and average cell density profile at 48 HPR projected onto the unit circle in dual SMAD + CHIR-treated colonies (n = 16 independent colonies).

See also Figures S3–S5.

neuroectoderm fates, consistent with its previously reported activity (Libby et al., 2020). By monitoring the trajectories of differentiating colonies at single-cell resolution, we detected morphogenic signatures at both the local-cell-neighborhood and the colony-wide level, thereby enabling quantitative measurement of the comprehensive dynamics of multicellular organization and subtle yet distinctive differences in cell behavior that distinguish between independent differentiation protocols.

DISCUSSION

Single-cell analyses have highlighted the intrinsic heterogeneity present in virtually all multicellular populations. Complementary approaches, such as automated cell lineage tracing and single-cell RNA sequencing, have enabled fine-grained spatiotemporal quantification of diverse and robust developmental processes (Bao et al., 2006; Cai et al., 2013; Mohammed et al., 2017). Understanding the dynamic behavior(s) of pluripotent stem cells in response to environmental factors can similarly clarify the effects of multicellular structure and environmental factors on the behavior and ultimate fate of individual cells within developing tissues and organs *ex vivo*. To assess how organization arises from the collective action of individual cells, we developed a dense-cell-tracking platform to analyze time-lapse imaging of hiPSC colonies with high spatiotemporal precision. Using the resulting quantitative measures of cell behaviors, we identified signatures of multicellular organization at the single-cell, local-neighborhood, and whole-colony scale, demonstrating that hiPSC behaviors are influenced by short-distance interactions between neighboring cells that propagate into global effects throughout an entire colony of hundreds of cells and more. While many of the measured cell-intrinsic properties were relatively constant under pluripotent culture and early differentiation conditions, we found that the local cell neighborhood responds in characteristic ways to different external stimuli. Changes in cell-cell interactions are orthogonal to stem cell pluripotency (Libby et al., 2018; Przybyla et al., 2016), but can have an impact on the sensitivity of hiPSCs to morphogenic cues (Libby et al., 2019), and thus may be a critical determinant in pre-patterning of cells to different cell fate decisions. The ability to specifically modulate cell-cell interactions through modification of culture conditions or genetic engineering provides new strategies to pre-pattern and control colony structure and subsequent differentiation trajectories (Libby et al., 2019). Furthermore, our live-cell monitoring platform during early differentiation allows for non-destructive, high-throughput assessment of regional changes in cell fate, providing a critical first step toward feedback control of hiPSC differentiation.

In this paper, we applied our tracking system to resolve human pluripotent morphogenesis evolution at single-cell resolution to the maintenance of hiPSCs and early differentiation, but it can be used more generally to quantify multicellular structure at scale with either static or time-lapse microscopy of any cell line. Quantitative comprehensive characterization of cellular neighborhood dynamics will provide a robust approach to interrogate the effects of multicellular interactions among a broad range of cell types across many species, and will provide novel metrics to assess the fidelity of stem cell models to recapitulate developmental processes in a tissue context *ex vivo*. Ultimately, extracting unbiased cell dynamics from *in vitro* time-lapse imaging enables new insights into the complex processes underlying multicellular organization and morphogenesis.

EXPERIMENTAL PROCEDURES

hiPSC colony formation and time-lapse imaging

The AICS-LMNB1 hiPSC cell line was maintained under feeder and serum-free, defined medium conditions in mTeSR1 (STEMCELL Technologies). hiPSCs were passaged and force aggregated as previously described (Hookway et al., 2016) for 24 h, then seeded into optically clear 96-well plates, and allowed to reattach for a further 24 h. Attached colonies were imaged at 10× on an Observer Z1 (Zeiss) spinning disc confocal microscope in both phase and GFP over the course of 6 h for pluripotent experiments, sampling every 3 min, or over 24 h for differentiation experiments, sampling every 5 min.

Neural net training

A time-lapse dataset of pluripotent colonies was manually segmented by human raters, who selected the center of mass of each cell nucleus in a shuffled and randomly rotated mixture of the frames of 12 time-lapse movies. Each neural net architecture was independently trained on 80% of the dataset, with performance evaluated each epoch on a 10% held-out test set, and final quality assessed on a 10% validation set. The top three performing nets were then averaged to form the final composite segmentation.

Cell tracking and colony metrology

The peaks of each composite cell detection were linked between sequential frames of each time-lapse movie, forming cell tracks, which were then used to estimate cell velocity, distance traveled, and other migration parameters. Within each frame, all detected cells in a colony were converted into a mesh using Delaunay triangulation, which was used to both estimate cell density and project each cell onto the radial bins defining the center, middle ring, or edge of the colony at each time point.

Statistical analyses

Except where noted, data are shown as the mean ± the 95% confidence interval assessed via bootstrap sampling. Statistical significance was assessed with ANOVA followed by two-tailed t tests with the Bonferroni-Holm correction for multiple comparisons,

with p value symbols reported as *p < 0.05, **p < 0.01, and ***p < 0.001. All statistical analyses were performed using the Python package statsmodels v.0.11.1.

See the supplemental experimental procedures for further details of cell culture protocols, training set generation, model evaluation, and tracking algorithm design and evaluation.

Data and code availability

Data, code, and trained model weights for the results reported in this paper are available at https://github.com/david-a-joy/deep-hipsc-tracking.

SUPPLEMENTAL INFORMATION

Supplemental information can be found online at https://doi.org/10.1016/j.stemcr.2021.04.008.

AUTHOR CONTRIBUTIONS

D.A.J., A.R.G.L., and T.C.M. conceptualized and designed the experiments. D.A.J. and A.R.G.L. performed the pluripotent cell culture and stem cell differentiations. D.A.J. performed the data acquisition, with advice from A.R.G.L. Neural network implementation, training, and evaluation were performed by D.A.J. The image analysis pipeline was designed, written, and executed by D.A.J. D.A.J. wrote the original manuscript with input from all co-authors. D.A.J. prepared the figures with input from all co-authors.

ACKNOWLEDGMENTS

We would like to thank our human annotators for their hard work segmenting hiPSC colony images. The authors would like to acknowledge funding support from the California Institute of Regenerative Medicine (LA1_C14-08015), and the National Science Foundation (CBET 0939511), awarded to T.C.M. In addition, we would like to acknowledge the Gladstone Stem Cell Core, the Gladstone Light Microscopy and Histology Core, and the Gladstone Graphics team for their invaluable technical support. Finally, we would like to specifically thank Dr. Kathrine Pollard for her analytical advice and expertise.

Received: October 30, 2020
Revised: April 14, 2021
Accepted: April 14, 2021
Published: May 11, 2021

REFERENCES

Araújo, F.H.D., Silva, R.R.V., Ushizima, D.M., Rezende, M.T., Carneiro, C.M., Campos Bianchi, A.G., and Medeiros, F.N.S. (2019). Deep learning for cell image segmentation and ranking. Comput. Med. Imaging Graph. *72*, 13–21.

Bao, Z., Murray, J.I., Boyle, T., Ooi, S.L., Sandel, M.J., and Waterston, R.H. (2006). Automated cell lineage tracing in Caenorhabditis elegans. Proc. Natl. Acad. Sci. U S A *103*, 2707–2712.

Barabási, A.-L., Albert, R., and Jeong, H. (1999). Mean-field theory for scale-free random networks. Phys. Stat. Mech. Appl. *272*, 173–187.

Cai, D., Cohen, K.B., Luo, T., Lichtman, J.W., and Sanes, J.R. (2013). Improved tools for the Brainbow toolbox. Nat. Methods *10*, 540–547.

Caicedo, J.C., Goodman, A., Karhohs, K.W., Cimini, B.A., Ackerman, J., Haghighi, M., Heng, C., Becker, T., Doan, M., McQuin, C., et al. (2019). Nucleus segmentation across imaging experiments: the 2018 data science bowl. Nat. Methods *16*, 1247–1253.

Chambers, S.M., Fasano, C.A., Papapetrou, E.P., Tomishima, M., Sadelain, M., and Studer, L. (2009). Highly efficient neural conversion of human ES and iPS cells by dual inhibition of SMAD signaling. Nat. Biotechnol. *27*, 275–280.

Chhetri, R.K., Amat, F., Wan, Y., Höckendorf, B., Lemon, W.C., and Keller, P.J. (2015). Whole-animal functional and developmental imaging with isotropic spatial resolution. Nat. Methods *12*, 1171–1178.

Cohen, J.P., Lo, H.Z., and Bengio, Y. (2017). Count-ception: counting by fully convolutional redundant counting. ArXiv, arXiv:1703.08710[cs.CV].

Cui, C., Yang, X., Chuai, M., Glazier, J.A., and Weijer, C.J. (2005). Analysis of tissue flow patterns during primitive streak formation in the chick embryo. Dev. Biol. *284*, 37–47.

Darnton, N.C., Turner, L., Rojevsky, S., and Berg, H.C. (2007). On torque and tumbling in swimming Escherichia coli. J. Bacteriol. *189*, 1756–1764.

Deglincerti, A., Croft, G.F., Pietila, L.N., Zernicka-Goetz, M., Siggia, E.D., and Brivanlou, A.H. (2016). Self-organization of the in vitro attached human embryo. Nature *533*, 251–254.

Devreotes, P., and Janetopoulos, C. (2003). Eukaryotic chemotaxis: distinctions between directional sensing and polarization. J. Biol. Chem. *278*, 20445–20448.

Falk, T., Mai, D., Bensch, R., Çiçek, Ö., Abdulkadir, A., Marrakchi, Y., Böhm, A., Deubner, J., Jäckel, Z., Seiwald, K., et al. (2019). U-Net: deep learning for cell counting, detection, and morphometry. Nat. Methods *16*, 67–70.

Glen, C.M., McDevitt, T.C., and Kemp, M.L. (2018). Dynamic intercellular transport modulates the spatial patterning of differentiation during early neural commitment. Nat. Commun. *9*, 4111.

He, T., Mao, H., Guo, J., and Yi, Z. (2017). Cell tracking using deep neural networks with multi-task learning. Image Vis. Comput. *60*, 142–153.

Henner, A., Ventura, P.B., Jiang, Y., and Zong, H. (2013). MADM-ML, a mouse genetic mosaic system with increased clonal efficiency. PLoS One *8*, e77672.

Hiramatsu, Y., Hotta, K., Imanishi, A., Matsuda, M., and Terai, K. (2018). Cell image segmentation by Integrating multiple CNNs. In 2018 IEEE/CVF Conference on Computer Vision and Pattern Recognition Workshops (CVPRW) (IEEE), pp. 2286–22866.

Hookway, T.A., Butts, J.C., Lee, E., Tang, H., and McDevitt, T.C. (2016). Aggregate formation and suspension culture of human pluripotent stem cells and differentiated progeny. Methods *101*, 11–20.

LeCun, Y., Bengio, Y., and Hinton, G. (2015). Deep learning. Nature *521*, 436–444.

Lian, X., Zhang, J., Azarin, S.M., Zhu, K., Hazeltine, L.B., Bao, X., Hsiao, C., Kamp, T.J., and Palecek, S.P. (2013). Directed

cardiomyocyte differentiation from human pluripotent stem cells by modulating Wnt/β-catenin signaling under fully defined conditions. Nat. Protoc. *8*, 162–175.

Libby, A., Joy, D., Elder, N., Bulger, E., Krakora, M., Gaylord, E., Mendoza-Camacho, F., Butts, J., and McDevitt, T. (2020). Elongation of Caudalized Human Organoids Mimics Neural Tube Development. bioRxiv https://doi.org/10.1101/2020.03.05.979732.

Libby, A.R., Joy, D.A., So, P.-L., Mandegar, M.A., Muncie, J.M., Mendoza-Camacho, F.N., Weaver, V.M., Conklin, B.R., and McDevitt, T.C. (2018). Spatiotemporal mosaic self-patterning of pluripotent stem cells using CRISPR interference. ELife *7*, e36045.

Libby, A.R.G., Briers, D., Haghighi, I., Joy, D.A., Conklin, B.R., Belta, C., and McDevitt, T.C. (2019). Automated design of pluripotent stem cell self-organization. Cell Syst. *9*, 483–495.e10.

Lou, X., Kang, M., Xenopoulos, P., Muñoz-Descalzo, S., and Hadjantonakis, A.-K. (2014). A rapid and efficient 2D/3D nuclear segmentation method for analysis of early mouse embryo and stem cell image data. Stem Cell Rep. *2*, 382–397.

Maiuri, P., Terriac, E., Paul-Gilloteaux, P., Vignaud, T., McNally, K., Onuffer, J., Thorn, K., Nguyen, P.A., Georgoulia, N., Soong, D., et al. (2012). The first world cell race. Curr. Biol. *22*, R673–R675.

Malmersjo, S., Rebellato, P., Smedler, E., Planert, H., Kanatani, S., Liste, I., Nanou, E., Sunner, H., Abdelhady, S., Zhang, S., et al. (2013). Neural progenitors organize in small-world networks to promote cell proliferation. Proc. Natl. Acad. Sci. U S A *110*, E1524–E1532.

Martinez Arias, A., and Steventon, B. (2018). On the nature and function of organizers. Development *145*, dev159525.

Moen, E., Bannon, D., Kudo, T., Graf, W., Covert, M., and Van Valen, D. (2019). Deep learning for cellular image analysis. Nat. Methods *16*, 1233–1246.

Mohammed, H., Hernando-Herraez, I., Savino, A., Scialdone, A., Macaulay, I., Mulas, C., Chandra, T., Voet, T., Dean, W., Nichols, J., et al. (2017). Single-cell landscape of transcriptional heterogeneity and cell fate decisions during mouse early gastrulation. Cell Rep. *20*, 1215–1228.

Novkovic, M., Onder, L., Cupovic, J., Abe, J., Bomze, D., Cremasco, V., Scandella, E., Stein, J.V., Bocharov, G., Turley, S.J., et al. (2016). Topological small-world organization of the fibroblastic reticular cell network determines lymph node functionality. PLoS Biol. *14*, e1002515.

Pegoraro, A.F., Fredberg, J.J., and Park, J.-A. (2016). Problems in biology with many scales of length: cell–cell adhesion and cell jamming in collective cellular migration. Exp. Cell Res. *343*, 54–59.

Peng, G., Suo, S., Chen, J., Chen, W., Liu, C., Yu, F., Wang, R., Chen, S., Sun, N., Cui, G., et al. (2016). Spatial transcriptome for the molecular annotation of lineage fates and cell identity in mid-gastrula mouse embryo. Dev. Cell *36*, 681–697.

Przybyla, L., Lakins, J.N., and Weaver, V.M. (2016). Tissue mechanics orchestrate wnt-dependent human embryonic stem cell differentiation. Cell Stem Cell *19*, 462–475.

Ronneberger, O., Fischer, P., and Brox, T. (2015). U-net: convolutional networks for biomedical image segmentation. In International Conference on Medical Image Computing and Computer-Assisted Intervention (Springer), pp. 234–241.

Shahbazi, M.N., and Zernicka-Goetz, M. (2018). Deconstructing and reconstructing the mouse and human early embryo. Nat. Cell Biol. *20*, 878–887.

Shahbazi, M.N., Jedrusik, A., Vuoristo, S., Recher, G., Hupalowska, A., Bolton, V., Fogarty, N.M.E., Campbell, A., Devito, L.G., Ilic, D., et al. (2016). Self-organization of the human embryo in the absence of maternal tissues. Nat. Cell Biol. *18*, 700–708.

Stegmaier, J., Amat, F., Lemon, W.C., McDole, K., Wan, Y., Teodoro, G., Mikut, R., and Keller, P.J. (2016). Real-time three-dimensional cell segmentation in large-scale microscopy data of developing embryos. Dev. Cell *36*, 225–240.

Su, H., Xing, F., Kong, X., Xie, Y., Zhang, S., and Yang, L. (2015). Robust cell detection and segmentation in histopathological images using sparse reconstruction and stacked denoising autoencoders. In Medical Image Computing and Computer-Assisted Intervention – MICCAI 2015, N. Navab, J. Hornegger, W.M. Wells, and A.F. Frangi, eds. (Springer International Publishing)), pp. 383–390.

Sulston, J.E., Schierenberg, E., White, J.G., and Thomson, J.N. (1983). The embryonic cell lineage of the nematode Caenorhabditis elegans. Dev. Biol. *100*, 64–119.

Szegedy, C., Liu, W., Jia, Y., Sermanet, P., Reed, S., Anguelov, D., Erhan, D., Vanhoucke, V., and Rabinovich, A. (2014). Going deeper with convolutions. ArXiv, arXiv:1409.4842[cs.CV].

Tewary, M., Ostblom, J., Prochazka, L., Zulueta-Coarasa, T., Shakiba, N., Fernandez-Gonzalez, R., and Zandstra, P.W. (2017). A stepwise model of reaction-diffusion and positional information governs self-organized human peri-gastrulation-like patterning. Development *144*, 4298–4312.

Turing, A.M. (1952). The chemical basis of morphogenesis. Philos. Trans. R. Soc. Lond. B Biol. Sci. *237*, 37–72.

Ulman, V., Maška, M., Magnusson, K.E.G., Ronneberger, O., Haubold, C., Harder, N., Matula, P., Matula, P., Svoboda, D., Radojevic, M., et al. (2017). An objective comparison of cell-tracking algorithms. Nat. Methods, 1141–1152.

Wang, Y., Mao, H., and Yi, Z. (2019). Stem cell motion-tracking by using deep neural networks with multi-output. Neural Comput. Appl. *31*, 3455–3467.

Warmflash, A., Sorre, B., Etoc, F., Siggia, E.D., and Brivanlou, A.H. (2014). A method to recapitulate early embryonic spatial patterning in human embryonic stem cells. Nat. Methods *11*, 847–854.

White, D.E., Kinney, M.A., McDevitt, T.C., and Kemp, M.L. (2013). Spatial pattern dynamics of 3D stem cell loss of pluripotency via rules-based computational modeling. PLoS Comput. Biol. *9*, e1002952.

Xie, W., Noble, J.A., and Zisserman, A. (2016). Microscopy cell counting and detection with fully convolutional regression networks. Comput. Methods Biomech. Biomed. Eng. Imaging Vis. *6*, 283–292.

Xie, Y., Xing, F., Shi, X., Kong, X., Su, H., and Yang, L. (2018). Efficient and robust cell detection: a structured regression approach. Med. Image Anal. *44*, 245–254.